Skin-friction drag reduction in a high-Reynolds-number turbulent boundary layer via real-time control of large-scale structures

M.R. Abbassi, W.J. Baars*, N. Hutchins, I. Marusic

Department of Mechanical Engineering, The University of Melbourne, Melbourne 3010, Victoria, Australia

ARTICLE INFO

Article history:
Available online 17 May 2017

Keywords:
Turbulent boundary layer
Flow control
Large-scale structure
Drag reduction

ABSTRACT

While large-scale motions are most energetic in the logarithmic region of a high-Reynolds-number turbulent boundary layer, they also have an influence in the inner-region. In this paper we describe an experimental investigation of manipulating the large-scale motions and reveal how this affects the turbulence and skin-friction drag. A boundary layer with a friction Reynolds number of 14 400 is controlled using a spanwise array of nine wall-normal jets operated in an on/off mode and with an exit velocity that causes the jets in cross-flow to penetrate within the log-region. Each jet is triggered in real-time with an active controller, driven by a time-resolved footprint of the large-scale motions acquired upstream. Nominally, the controller injects air into large-scale zones with positive streamwise velocity fluctuations; these zones are associated with positive wall-shear stress fluctuations. This control scheme reduced the streamwise turbulence intensity in the log-region up to a downstream distance of more than five times the boundary layer thickness, δ, from the point of actuation. The highest reduction in spectral energy—more than 30%—was found for wavelengths larger than 5δ in the log-region at 1.7δ downstream of actuation, while scales larger than 2δ still comprised more than 15% energy reduction in the near-wall region. In addition, a 3.2% reduction in mean skin-friction drag was achieved at 1.7δ downstream of actuation. Our reductions of the streamwise turbulence intensity and mean skin-friction drag exceed a base line control-case, for which the jet actuators were operated with the same temporal pattern, but not synchronised with the incoming large-scale zones of positive fluctuating velocity.

1. Introduction

Wall-bounded flows are important to many natural and engineering applications, and given that skin-friction drag constitutes approximately 50%, 90% and 100% of the total drag on airliners, submarines and pipelines, respectively (Gad-el Hak, 1994), considerable effort has been devoted to reducing skin-friction drag over the past few decades.

Over the past 50 years or so it has been shown that turbulent boundary layers (TBLs) comprise coherent structures in both the near-wall and outer regions (Kline et al., 1967; Townsend, 1976; Kim and Moin, 1979; Robinson, 1991; Wark and Nagib, 1990; Adrian et al., 2000; Smits and Marusic, 2013). The majority of flow control studies with the aim of skin-friction drag reduction have attempted to manipulate structures within the near-wall region (Moin and Bewley, 1994; Gad-el Hak, 2000; Rathnasingham and Breuer, 1997; 2003; Karniadakis and Choi, 2003; Kasagi et al., 2009; Gouder et al., 2013; Bai et al., 2014, among others). These near-wall structures scale with viscous units, being the friction velocity $U_\tau \equiv \sqrt{\tau_w/\rho}$, where τ_w is the mean wall-shear stress and ρ is the fluid density, and inner length scale ν/U_τ, with ν being the fluid kinematic viscosity; note that superscript '+' denotes scaling with inner-variables. As such, most of the aforementioned studies tailored their control parameters in viscous-scaled units. However, when increasing the Reynolds number to more pragmatic values, the range of energetic turbulent scales grows, conceptually bounded by the outer (δ, the boundary layer thickness) and inner (ν/U_τ) length scales. We here use the friction Reynolds number, $Re_\tau \equiv \delta U_\tau/\nu$, to indicate the state of the TBL. At high, practical values of Re_τ, the physical thickness of the near-wall region and hence the size of the structures populating that region become smaller (Head and Bandyopadhyay, 1981; Robinson, 1991; Gad-el Hak and Bandyopadhyay, 1994). Due to the characteristic length [$\mathcal{O}$(μm)] and time [$\mathcal{O}$(μs)] scales in engineering applications ($Re_\tau \sim 10^4 - 10^6$), one needs to deal with micro-electro-mechanical systems (MEMS) for control. Both the development and operation of these sensors become demanding. At the same time, the performance of control schemes solely manipulating the near-wall region deteriorates with increasing Re_τ (Chang et al., 2002; Iwamoto et al., 2002; Gatti and Quadrio, 2013; Hurst et al., 2014).

* Corresponding author.
E-mail address: wbaars@unimelb.edu.au (W.J. Baars).

http://dx.doi.org/10.1016/j.ijheatfluidflow.2017.05.003
0142-727X/© 2017 Elsevier Inc. All rights reserved.

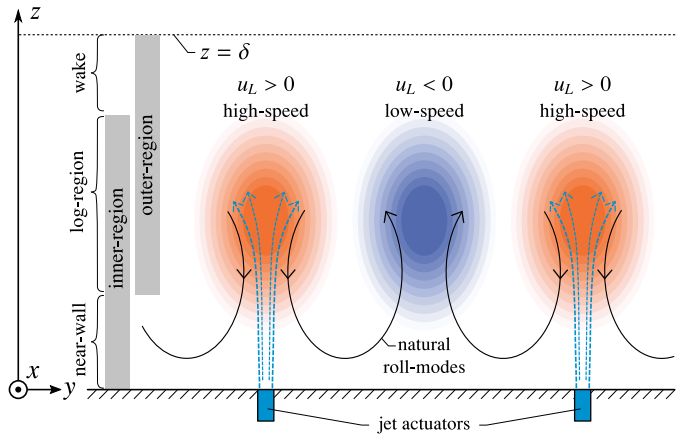

Fig. 1. Schematic of coherent streamwise flow motion in the spanwise–wall-normal plane of a high-Reynolds-number TBL. Regions with positive and negative streamwise velocity fluctuations are referred to as high- and low-speed zones, respectively. Associated natural roll-modes are indicated by the arrows. An illustration of opposition control is shown using wall-jet actuators.

An alternative approach to targeting the near-wall small-scale motions is to use a large-scale forcing scheme, as investigated in the seminal work by Schoppa and Hussain (1998) for a direct numerical simulation of a turbulent channel flow up to $Re_\tau \approx 180$. A drag reduction of up to 50% was demonstrated (using spanwise jets as a large-scale flow forcing), which was interpreted as a result of weakened longitudinal vortices near the wall, due to forcing-induced suppression of an underlying streak instability mechanism. Recently it was shown that the reported drag reduction in Schoppa and Hussain (1998) is associated with a transient nature of the flow due to the low values of Re_τ at which the turbulence is marginally sustainable (Canton et al., 2016). Moreover, Canton et al. (2016) concluded that inducing large-scale vortices for drag reduction becomes ineffective at their highest Reynolds number ($Re_\tau \approx 550$). Nevertheless, the question remains whether a large-scale control scheme can generate skin-friction drag reduction at higher Reynolds numbers, $Re_\tau > \mathcal{O}(10^4)$. Under these conditions, the large-scale motions (LSMs) and very large-scale motions (or superstructures) become the dominant contributor to the turbulent kinetic energy and its production (Hutchins and Marusic, 2007b; 2007a; Marusic et al., 2010a). For reference, when considering a pre-multiplied energy spectrogram of the streamwise velocity fluctuations (energy per wavelength throughout the TBL), the appearance of a broad spectral peak in the log-region reflecting the LSMs, is only observed for moderate Reynolds numbers (roughly $Re_\tau > 2000$ Hutchins and Marusic, 2007a). While LSMs are most energetic in the log-region at high Re_τ, they also have an influence in the near-wall region (*e.g.* Abe et al., 2004) via a direct superposition of large-scale energy and an amplitude modulation of the smaller scales (Hutchins and Marusic, 2007a; Marusic et al., 2010b). It is therefore hypothesised that controlling the LSMs at high Re_τ affects the near-wall turbulence and has the potential of reducing the mean and fluctuating components of the wall-shear stress.

Large-scale structures in the log-region can simplistically be represented as long elongated regions with a streamwise extent of $\mathcal{O}(\delta)$, comprising streamwise momentum deficit. These regions are flanked on either spanwise side by zones of streamwise momentum surplus (*e.g.* Adrian et al., 2000). The former and the latter structures are referred to as low- and high-speed zones, respectively, and are schematically shown in a spanwise–wall-normal plane in Fig. 1. Here we denote the large-scale streamwise velocity fluctuation with u_L, so that $u_L > 0$ and $u_L < 0$ indicate high- and low-speed zones. Accompanying these large-scale zones are counter-rotating roll-modes, with the respective up- and down-wash sections embodied within the low- and high-speed zones as indicated in Fig. 1 (*e.g.* Dennis and Nickels, 2011; Hutchins et al., 2012).

The aim of the present experimental investigation is to manipulate the large-scale high- and low-speed zones in real-time. For this we employ a control architecture embedded in the high-Reynolds-number boundary layer facility in Melbourne, which is introduced in Section 2. The hardware includes surface-embedded actuators, which can inject a wall-normal jet flow into the TBL so that the jets in cross-flow penetrate within the log-region. We nominally explore an opposition control framework, meaning that the actuators are activated while a high-speed zone is present. This results in the wall-normal jet flow opposing the down-wash sections of the naturally occurring roll-modes and the injection of fluid—without streamwise momentum—into the zone with a naturally positive velocity fluctuation (see Fig. 1). How the control affects the downstream flow in the log-region is presented in Section 3, after which we present a detailed boundary layer survey and wall-drag characterisation in Section 4.

2. Experimental arrangement

2.1. Facility and conditions

Experiments were conducted in the boundary layer facility at the University of Melbourne (Nickels et al., 2005; Baars et al., 2016b). A 27 m long test section ensures the formation of a high-Reynolds-number boundary layer over the wind tunnel floor, while high spatial and temporal resolutions are obtained with existing instrumentation under moderate free-stream velocities. For a zero-pressure gradient configuration, the pressure coefficient is constant to within ± 0.87% (Marusic et al., 2015) and free-stream turbulence intensities are less than 0.05% at the test section inlet. An isometric sketch of the wind tunnel, with an open-view of the test section, is shown in Fig. 2a. A coordinate system with coordinates x, y and z denotes the streamwise, spanwise and wall-normal directions of the flow, respectively, and its origin coincides with the test section inlet, the wall and spanwise centre of the tunnel.

Real-time control of the TBL was performed at a streamwise location that nominally coincided with a floating element drag balance (permanently embedded within the wind tunnel surface). This large-scale floating element drag balance, with a streamwise length $l_F = 3.000$ m and a spanwise width $w_F = 1.000$ m, is centred at $x = x_F = 21.00$ m and $y = 0$. The modular design of the flow-exposed surface of the drag balance allowed for an implementation of the control hardware, whereas directly measured wall drag data at local Reynolds numbers (Baars et al., 2016b) provided the nominal experimental conditions and assisted in calibration of hot-film sensors (discussed later on in Section 2.4). Throughout this paper, one flow condition is considered, corresponding to a nominal free-stream velocity of $U_\infty = 20$ m/s. At $x = 21.00$ m this provides a boundary layer thickness of $\delta = 0.360$ m and a friction velocity of $U_\tau = 0.641$ m/s, resulting in $Re_\tau \approx 14\,400$. These parameters were determined by fitting a composite velocity profile of Chauhan et al. (2009) to the mean velocity profile, with log-law constants $\kappa = 0.384$ and $A = 4.17$. From friction data measured with the floating element drag balance (Baars et al., 2016b), a value of $U_\tau = 0.649$ m/s is obtained, which agrees to within 1.2% with the value found via the composite profile fit. A summary of the nominal flow conditions and TBL is provided in Table 1; here, subscript 'U' in U_{τ_U} refers to an uncontrolled TBL flow. Finally, throughout this paper, we employ a location in the log-region that reflects the location of the outer-peak in the pre-multiplied energy spectrogram under similar conditions (Mathis et al., 2009), taken as $z_L^+ \equiv 3.9\sqrt{Re_\tau} \approx 477$. At this position, the

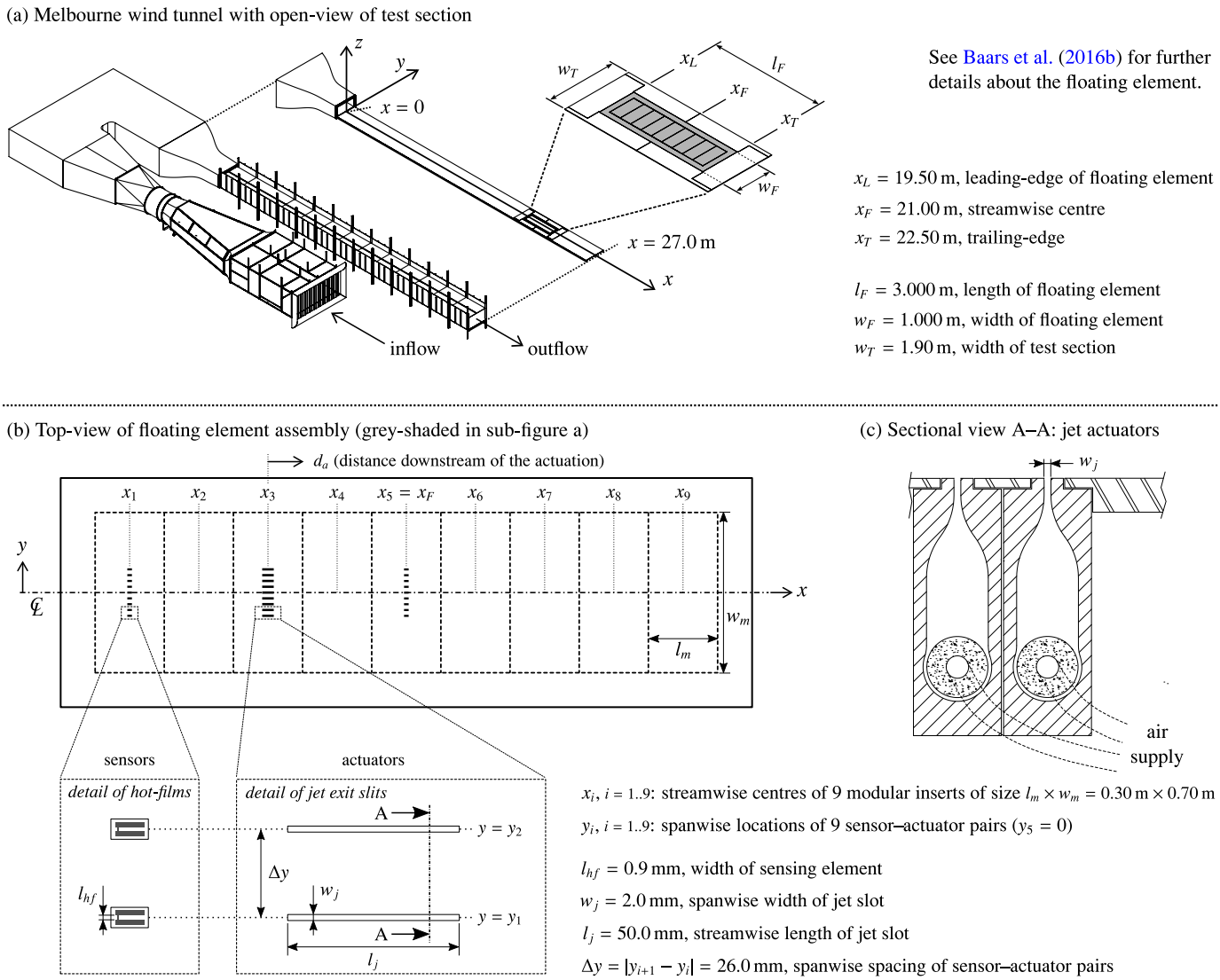

Fig. 2. (a) Schematic of the boundary layer facility at the University of Melbourne with an open view (sidewalls and ceiling removed) of the test section, indicating the floating element assembly (Baars et al., 2016b). (b) Top-view of the floating element assembly with the real-time control hardware implemented in the wind tunnel surface. (c) Cross-sectional view A–A, indicated in sub-figure (b), of the jet actuators.

Table 1
Flow conditions and sensor specifications for the experimental campaign in the high-Reynolds-number boundary layer facility at Melbourne.

Conditions for the *uncontrolled* TBL flow								Hot-wire sensor				Hot-film sensor		
x (m)	Re_τ	Re_θ	δ (m)	U_∞ (m/s)	U_{τ_U} (m/s)	ν/U_{τ_U} (μm)	$\nu/U_{\tau_U}^2$ (μs)	l_{hw}^+	l_{hw}/d	$1/\Delta t$ (Hz)	Δt^+	l_{hf}^+	$1/\Delta t$ (Hz)	Δt^+
21.00	14 400	44 000	0.360	20.27	0.639	24.95	39.04	20	200	20 000	1.32	36	4 000	6.62

mean streamwise velocity is $U_c^+(x_F, z_L^+) \approx 21.7$, which is an approximate convection velocity for the large-scale structures (Baars et al., 2014).

All components of the control set-up were implemented on the floating element. Its flow-exposed surface of $l_F \times w_F$ is grey-shaded in Fig. 2a and a top-view is shown in Fig. 2b. Nine removable panels (dashed lines), each measuring $l_m = 0.30$ m in x and $w_m = 0.70$ m in y, form a modular construction. Locations $x_1 = 19.80$ m to $x_9 = 22.20$ m indicate the streamwise centres of all inserts. The sensors and actuators embedded on these panels are discussed next.

2.2. Control architecture

2.2.1. Sensing: turbulent boundary layer footprint

We employ an active control framework (Section 2.3) for which flow actuation takes place downstream of the location where the LSMs are sensed. Monitoring the passage of the high- and low-speed zones at one streamwise location can be achieved via a spanwise rake of hot-wires (*e.g.* Hutchins and Marusic, 2007a), but this would significantly alter the flow. Previous studies have shown that a strong coherence exists between the large-scale fluctuations in the log- and inner-regions of the flow (Johansson and Alfredsson, 1982; Abe et al., 2004; Marusic et al., 2010b; Baars et al., 2016a, among others). As such, surface-mounted hot-film

Table 2
Positions and dimensions of the nine sensor–actuator pairs used for flow control. Flow conditions for the experimental campaign, at a friction Reynolds number of $Re_\tau \approx 14\,400$, are indicated in Table 1.

Array		Location		Properties			
		x (m)	y (mm)	l_{hf}	l_j	w_j	Δy
sensors	s_1 & s'_1	$x_1 = 19.80$ & $x_5 = 21.00$	$y_1 = -104$	$l^+_{hf} = 36$	–	–	$\Delta y^+ = 1042$
	s_2 & s'_2		$y_2 = -78$				
	s_3 & s'_3		$y_3 = -52$				
	s_4 & s'_4		$y_4 = -26$				
	s_5 & s'_5		$y_5 = 0$				
	s_6 & s'_6		$y_6 = 26$				
	s_7 & s'_7		$y_7 = 52$				
	s_8 & s'_8		$y_8 = 78$				
	s_9 & s'_9		$y_9 = 104$				
actuators	a_1	$x_3 = 20.40$	$y_1 = -104$	–	$l^+_j = 2004$	$w^+_j = 80$	$\Delta y^+ = 1042$
	a_2		$y_2 = -78$				
	a_3		$y_3 = -52$				
	a_4		$y_4 = -26$				
	a_5		$y_5 = 0$				
	a_6		$y_6 = 26$				
	a_7		$y_7 = 52$				
	a_8		$y_8 = 78$				
	a_9		$y_9 = 104$				

sensors are employed to measure the wall-shear stress fluctuations as surrogates of the streamwise velocity fluctuations in the log-region. A spanwise array of nine Dantec skin-friction sensors (model 55R47) were attached to one panel insert, located at $x_1 = 19.80$ m (Fig. 2b). A spanwise spacing of the sensors was adopted from the study by Hutchins et al. (2011) and equals $\Delta y = 26.0$ mm ($\Delta y^+ \approx 1042$ or $\Delta y/\delta = 0.072$) and the sensor-array was placed in the spanwise centre of the panel insert; note that nine actuators are located in-line, downstream of the nine sensors (Section 2.2.2), forming nine sensor–actuator pairs. Each hot-film has a sensing element of 0.1 × 0.9 mm (in x and y directions, respectively), which equates to an active spanwise sensor length of $l^+_{hf} = 37$ (see *detail of hot-films* inset in Fig. 2b). Wall-normal steps associated with these glue-on type sensors are generally less than $3.5\nu/U_{\tau_U}$ (Hutchins et al., 2011) and can therefore be considered as hydraulically smooth ($k^+_s \lesssim 4$, following Nikuradse, 1933). A 9-channel (AA Lab Systems AN-1003) constant-temperature anemometer (CTA) with an overheat ratio of 1.05 was used to operate the sensors. Aside from the sensor-array at $x_1 = 19.80$ m, a duplicate array (with a separate 9-channel CTA) was positioned at $x_5 = 21.00$ m (Fig. 2b). This sensor-array was not used for control, but was used to survey the controlled flow (Section 2.4). Positions and relevant dimensions of the nine sensors forming the arrays at both x_1 and x_5 (s_1–s_9 for x_1 and s'_1–s'_9 for x_5) are summarised in Table 2.

Wall-shear stress fluctuations are only resolved up to a cut-off frequency of roughly 80 Hz due to sensor limitations (Hutchins et al., 2011). For the purpose of our large-scale manipulation this bandwidth is sufficient (a large-scale filter is discussed in Section 2.3), since $f = 80$ Hz equates to a spatial wavelength of $\lambda_x \equiv U_c/f \approx 0.48\delta$.

2.2.2. Actuation: wall-normal jets

As noted before, nine actuators are located in-line, downstream of sensors $s_1 - s_9$, to form nine sensor–actuator pairs. The spanwise array of actuators was embedded in a panel located at $x_3 = 20.40$ m. Our present actuators are wall-normal jets with rectangular exit slits, each measuring $l_j \times w_j = 50.0 \times 2.0$ mm, and are aligned in the streamwise direction (see *detail of jet exit slits* inset in Fig. 2b). In inner- and outer-length-scales, dimensions are $l^+_j \times w^+_j \approx 2004 \times 80$ and $l_j/\delta \times w_j/\delta \approx 0.139 \times 0.006$, respectively. Regarding location, the sensor-array is located $|x_3 - x_1| \approx 1.7\delta$ downstream of the sensor-array (locations of actuators a_1–a_9 are listed in Table 2). For two adjacent actuators we have shown a cross-section in Fig. 2c. Each jet cavity accommodates a cylindrical polyethylene porous silencer, through which compressed air is supplied via 80 cm long hoses from a Festo MPAL-IV solenoid valve terminal. Upstream of these valves is a pressure regulator, set at approximately 0.8 bar, and a compressor and reservoir that provide the required flow rate to operate our control set-up in a continuous manner. The supply pressure and porous silencer ensure that the jet exit velocity profile, in the absence of any TBL flow, has a mean velocity of $V_j \approx 12.9$ m/s ($V_j/U_\infty \approx 0.64$ and $V^+_j = 20.2$) and is uniform along the streamwise length of the slit to within ±2.5%. Note that V_j corresponds to continuous operation of five actuators and that the exit velocity was chosen so that the jets in cross-flow penetrated within the log-region (see Section 4). All jet actuators are operated in an on/off mode, meaning that each jet is triggered by a control logic (Section 2.3) and operates continuously when switched on. Nominally-closed solenoid valves are opened via 24 V relay switches, triggered by TTL control signals. A mechanical latency for the actuators was measured as $\tau_m = 14.3$ ms and corresponds to the time span from commanding the valve to open and the jet velocity reaching V_j; this delay was determined from conditionally averaging a time-resolved jet exit velocity on the trigger command.

2.2.3. Real-time controller and sampling

A Speedgoat performance real-time target machine with an Intel core 2 Duo 3.33 GHz processor, with dedicated 4096MB DDR2 memory, was used as hardware for executing our active control (Section 2.3), implemented via MathWorks Simulink Real-Time in an xPC target environment. A 16-bit A/D conversion via an IO106 Speedgoat module allowed for simultaneous sampling of all 22 sensors (generally two arrays of 9 hot-films each, a hot-wire, ambient pressure, temperature and free-stream dynamic pressure). The controller's sampling rate was set at $\Delta t = 0.25$ ms, corresponding to a frequency of $f_c = 4000$ Hz. Implementation of our control logic on the target machine resulted in a task execution time (TET) of less than 0.20 ms (the time it takes to accomplish one iteration through the control diagram). Real-time control was feasible due to the controller's sampling rate being more than 25% larger. Hot-film signals were acquired at the controller frequency f_c, although the signal of a hot-wire (Section 2.4) was simultaneously acquired at a faster sampling rate. Output commands to the 24 V relays, for

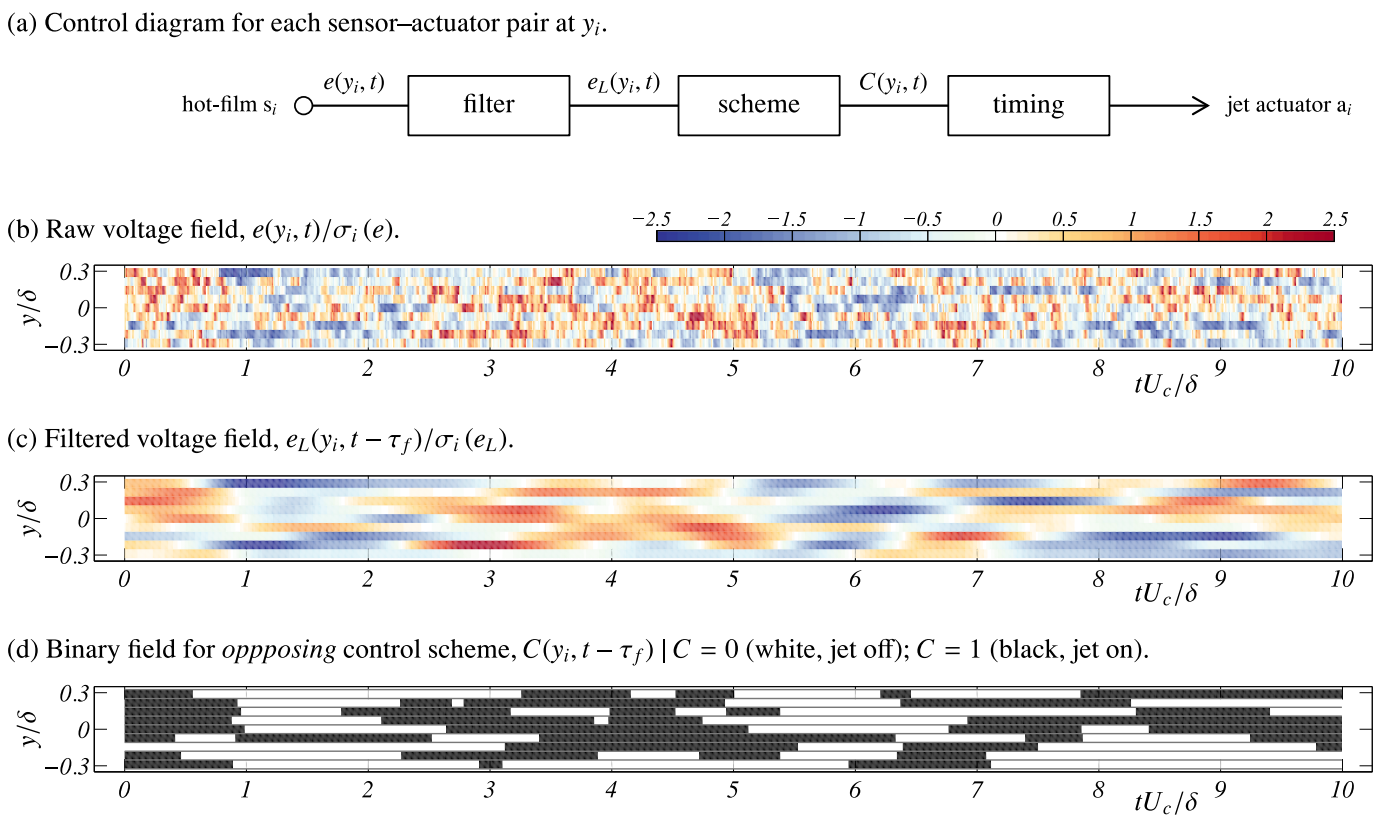

Fig. 3. (a) Control diagram for each of the nine sensor–actuator pairs. (b) Sample time segment of the raw fluctuating voltage signals of the sensor-array, shown as a contour for the nine actuator locations in y and a duration of 10 boundary layer turn-over times. (c) Large-scale filtered voltage signals corresponding to the signals shown in sub-figure (b). (d) Binary field corresponding to the large-scale fluctuating signals shown in sub-figure (c) for the *opposing* control scheme.

switching the solenoid valves, were sent via an IO205 Speedgoat module.

2.3. Control logic and implementation

In this section we describe the implemented control logic, consisting of three general steps (Fig. 3a): large-scale filtering, imposing a control scheme and timing the actuation in-sync with the convecting flow. At this point it is worth noting that the control logic is the same for each sensor–actuator pair, s_i–a_i at spanwise location y_i.

2.3.1. Large-scale filter

Time segments of the raw voltage signals of sensors s_1–s_9 are visualised in Fig. 3b and denoted as $e(y_i, t)$; note that the amplitude of these zero-mean fluctuations at each of the nine discrete locations y_i have been normalised by their respective standard deviations $\sigma_i(e)$. In order to retrieve the large-scale fluctuations, $e_L(y_i, t)$, a Gaussian filter was convoluted with each signal in real-time. The Gaussian filter of six standard deviations in length spanned $1.5 f_c \delta / U_c \approx 166$ samples in terms of the controller's sampling rate (here a slightly larger δ of 0.369 m was assumed). The Gaussian filter is simplistically characterised as a low-pass filter with a cut-off wavelength $\lambda_{xF} \approx 1.9\delta$, defined as the scale beyond which the magnitude response drops below 0.707 (we transformed frequency to wavelength using Taylor's hypothesis). Note that λ_{xF} is larger than the 0.48δ small-wavelength limitation of the sensors (Section 2.2.1), hence, the signals $e_L(y_i, t)$ adequately reflect a footprint of the LSMs. Aside from the large-scale Gaussian filter, a running mean filter compensated drift of the hot-film signals; this running mean of 10 s (40 000 samples) was subtracted from the signals in real-time and our implementation accounted for initialization time of the filters. A time segment of the large-scale filtered voltage signals, corresponding to the raw signals shown in Fig. 3b, is shown in Fig. 3c. Furthermore, implementation of the large-scale filter in real-time introduces a time delay of half the Gaussian width ($\tau_f \approx 20.8$ ms), which is accounted for in the visual of Fig. 3c so that the raw and filtered fields align.

2.3.2. Control scheme

Three control schemes were investigated for manipulating the LSMs. Nominally, an opposition control framework (recall Fig. 1 and its description) requires actuation of the jets at instances of high-speed zones. This control scheme is referred to as an *opposing* scheme and a so-called binary field is formed from $e_L(y_i, t)$, following

$$C(y_i, t) = \begin{cases} 1, & e_L(y_i, t) > 0 \\ 0, & e_L(y_i, t) < 0 \end{cases} \tag{1}$$

Here, $C(y_i, t)$ is the binary field (serving as the TTL signals controlling the valves, Section 2.2.3), which is either one- or zero-valued; a contour of $C(y_i, t)$ is shown in Fig. 3d, corresponding to the large-scale filtered field $e_L(y_i, t)$. It is worth noting that, on average, the actuators are on for 50% of the time, since our on/off control is based on the sign of the large-scale fluctuations (this avoids having to calibrate the sensor-array for control).

Aside from the *opposing* control, two additional schemes were implemented. A base line case constitutes a scenario for which the same amount of jet fluid would be injected into the TBL, but not in-sync with large-scale high-speed zones; we refer to this case as *desynchronised* control. Practically, a set of pre-recorded binary signals from the *opposing* control scheme triggered the actuator-array, independent of the upstream input signals. A third control scheme

Table 3
Definitions and naming of the control schemes.

Case	Scheme	$e_L > 0$	$e_L < 0$	Subscript
Uncontrolled	n/a	$C = 0$	$C = 0$	U
Controlled	Desynchronised (see the text)			D
	Opposing	$C = 1$	$C = 0$	O
	Reinforcing	$C = 0$	$C = 1$	R

is dubbed *reinforcing* control and is the inverse of the *opposing* control in the sense that the jet actuators are activated at instances of low-speed zones. A summary of the control schemes is provided in Table 3.

2.3.3. Timing of actuation

Implementation of our feed-forward active control strategy imposes time delays, which inherently requires a finite distance between the sensor- and actuator-arrays. That is, a time delay accumulates from the mechanical activation of the jet flow ($\tau_m \approx$ 14.3 ms, Section 2.2.2), real-time large-scale filtering ($\tau_f \approx 20.8$ ms, Section 2.3.1) and a single controller time step ($\tau_c = 0.25$ ms). For the streamwise separation between sensing and actuation ($\Delta x =$ 0.60 m) the convection velocity of the large-scale footprint is well-approximated by U_c (recall that U_c is the mean streamwise velocity in the log-region at z_L, see Section 2.1). Because we aim to manipulate the LSMs in the log-region, while measuring their imprint at the wall, their characteristic forward leaning structure needs to be accounted for. Typically, forward inclination angles of $\theta \approx 16°$ have been reported for the u component of velocity (Hutchins et al., 2012). The temporal lead of the LSMs in the log-region, relative to their footprint, has been empirically determined as the maximum in the temporal two-point correlation between hot-film s_5 and a hot-wire in the log-region. The latter was positioned directly above the hot-film at a position closely resembling the geometric centre of the log-region (Marusic et al., 2013), $z^+ \approx 900$, resulting in a temporal lead of $\tau_i \approx 8.0$ ms. Actuators are now timed in such a way that the jet exit velocity reaches full-flowing conditions when the LSMs at $z^+ \approx 900$ are estimated to appear at the streamwise location of the actuators. For this synchronization to occur, an extra output delay (τ_e) may have to be implemented in the controller, which equals the convection time of the LSMs ($\Delta x/U_c$), accounting for their forward leaning structure, minus the sum of the aforementioned time delays. Our current conditions provide

$$\tau_e = \frac{\Delta x}{U_c} - \tau_i - \left(\tau_m + \tau_f + \tau_c\right) \approx -0.2 \text{ ms}, \tag{2}$$

meaning that the actuation is 0.2 ms too late. Since only a positive time delay can physically be implemented in real-time, no extra delay has been imposed ($\tau_e = 0$ in practice). A 0.2 ms timing inaccuracy is insignificant in terms of the large-scale control (0.2 ms corresponds to a scale less than 0.01δ and is less than one time step of the controller). When control experiments were performed with a deliberately imposed delay ($\tau_e > 0$), effectiveness of the *opposing* control scheme was found to deteriorate with increasing τ_e, which suggests that our timing ($\tau_e = 0$) was optimum for the current hardware configuration.

Although the correct timing of the active control is guaranteed, the separation distance between the sensor- and actuator-arrays results in an inaccuracy related to the inapplicability of Taylor's hypothesis. That is, our first-principal implementation of the control assumes that the footprint of the LSMs is frozen when convecting from the sensors to actuators. Baars et al. (2014) determined (with a second sensor-array at the location of the current actuator-array) that the on/off control is 68.3% accurate in terms of timing. Hence, both the *opposing* and *reinforcing* control schemes are subject to this inaccuracy. Future extensions of the control set-up may include estimation procedures that more optimally predict the evolution of the LSMs (see for instance Rathnasingham and Breuer, 2003).

2.4. Measuring the effects of control

Measurements were made downstream of the actuator-array in order to examine the effects of control. A single hot-wire sensor was mounted at $y = 0$ on a traverse that could be moved in streamwise and wall-normal directions. A platinum wire with a diameter $d = 2.5$ μm and an exposed sensing element with a length-to-diameter ratio of $l_{hw}/d = 200$ (recommended by Ligrani and Bradshaw, 1987) provided a viscous-scaled spanwise wire length of $l^+_{hw} \approx 20$. An in-house built anemometer (MUCTA) operated the hot-wire in CTA mode and a sampling rate of $\Delta t^+ \approx 1.32$ guaranteed an absence of temporal attenuation (Hutchins et al., 2009). Signals were acquired for a duration of approximately $20\,300\delta/U_\infty$ at each hot-wire position (spectral statistics are converged at the largest energetic wavelengths). Before and after measurements, the hot-wire probe was calibrated against a Pitot-static tube (Talluru et al., 2014).

An array of nine hot-films—different than the one serving as controller-input—was positioned at $x_5 = 21.00$ m (Section 2.2.1); note that these hot-films were not necessarily sampled together with the hot-wire. Hot-film signals were acquired at the controller sampling rate, resulting in $\Delta t^+ \approx 6.62$. Twenty realizations of 180 s each were acquired for the *uncontrolled* flow and all three control schemes (a total of roughly $202\,700\delta/U_\infty$ data for each of the four cases). This array of hot-films was calibrated *in situ* in order to obtain absolute values of the skin-friction drag (used in Section 4.4 to assess the change in skin-friction drag due to control). Details of the calibration procedure can be found in Appendix A.

3. Streamwise recovery of the controlled flow

Here we examine the streamwise evolution of the TBL flow subject to the *opposing* control scheme; we focus at a position in the log-region, $z^+_L \equiv 3.9\sqrt{Re_\tau} \approx 477$. The measurements were acquired with the single hot-wire at $y = 0$ and $z = z_L$. A total of six streamwise positions were considered, and coincided with the streamwise centres of the six panel inserts downstream of the actuator-array (Fig. 2b). A new streamwise coordinate, d_a, is defined as the distance downstream of the actuator-array ($d_a \equiv x - x_3$; recall that actuation was at $x = x_3$). Fig. 4 presents the percentage change in both the mean streamwise velocity and turbulence intensity (energy) of the streamwise velocity fluctuations, induced by the *opposing* control scheme relative to the *uncontrolled* flow. It is apparent that the mean streamwise velocity has been reduced, although this effect relaxes from a difference of approximately −4.5% to −2.6% for $d_a/\delta \approx 0.8 \rightarrow 5.0$ (note that $d_a/\delta \approx 5.0$ equates to 72 000 inner length scales). The reduction in mean velocity is most likely caused by the wall-normal jet flows, which do not contain any streamwise momentum when passing through the jet exit planes. The percentage change in the variance of u demonstrates a 10.1% reduction due to control at $d_a/\delta \approx 0.8$ and a larger reduction of 14.2% at $d_a/\delta \approx 1.7$, beyond which the effect of control decays. In order to discuss this trend we present the corresponding pre-multiplied energy spectra at these six locations in Fig. 5a. Note that for our temporal data we transform frequency to wavelength using Taylor's hypothesis, where the local mean velocity is taken as the convection velocity. At wavelengths larger than the approximate cut-off wavelength used in our large-scale control ($\lambda_x > \lambda_{xF}$) a monotonic recovery of the spectral energy appears with increasing distance downstream of the actuation. For the smaller

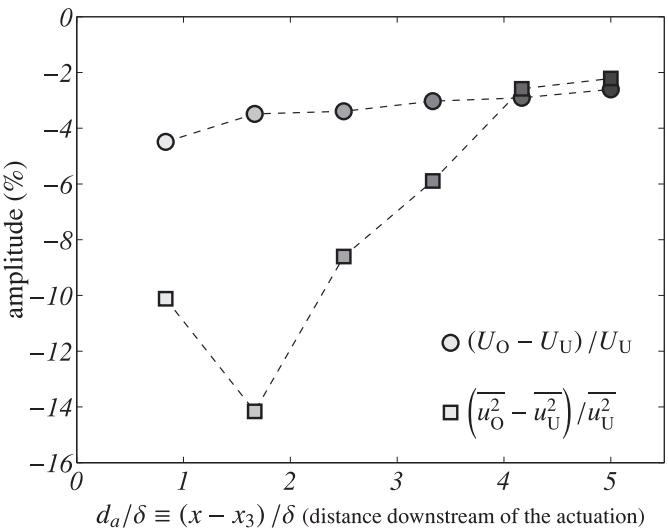

Fig. 4. Streamwise evolution of the percentage change in the mean and variance of the streamwise velocity fluctuations (due to the *opposing* control scheme, relative to the *uncontrolled* flow) at $z_L^+ \equiv 3.9\sqrt{Re_\tau} \approx 477$ and $y = 0$.

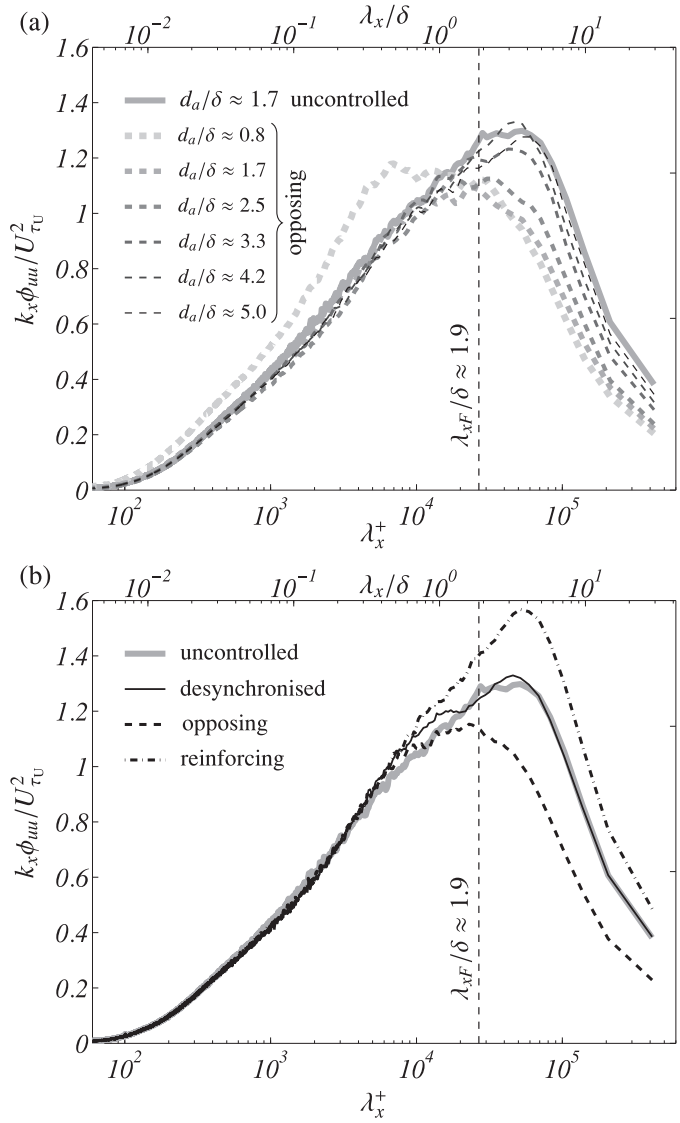

Fig. 5. (a) Streamwise evolution of the pre-multiplied energy spectra of the streamwise velocity fluctuations, $k_x\phi_{uu}/U_{\tau_U}^2$, corresponding to the variance-curve in Fig. 4. (b) Pre-multiplied energy spectra of the streamwise velocity fluctuations at $z_L^+ \approx 477$, $d_a/\delta \approx 1.7$ and $y = 0$ for the *uncontrolled* flow and three control schemes. The vertical dashed line marks the cut-off wavelength corresponding to the large-scale filter (described in Section 2.3.1).

scales however ($\lambda_x < \lambda_{xF}$), most of the spectra collapse (*uncontrolled* and *opposing* controlled flow) except for the closest location to the actuation, being $d_a/\delta \approx 0.8$. For this location we attribute the substantial increase in the spectral energy of these smaller scales to the small-scale turbulence introduced by the actuator jets interacting with the TBL. Since the addition of small-scale energy seems to dissipate faster than the recovery-effect of the suppression of the large-scale energy, a minimum in the variance profile of Fig. 4 is explained. Before proceeding with detailed surveys of the entire boundary layer at this streamwise location ($d_a/\delta \approx 1.7$) we consider energy spectra for all control schemes at $d_a/\delta \approx 1.7$ and $z = z_L$. These spectra are shown in Fig. 5b and indicate that for the *desynchronised* control scheme the overall energy across scales shows negligible change with respect to that of the *uncontrolled* flow. In line with Fig. 5a, for the *opposing* control scheme, there is a significant energy decrease for $\lambda_x/\delta \gtrsim 1$, which seems to suggest that the *opposing* scheme is successfully targeting and mitigating large-scale energy. For the *reinforcing* control scheme, an enhancement of energy with respect to the *uncontrolled* case is observed at the large wavelength-end of the spectrum. In summary, it can be concluded that for the *opposing* control case, where the jet actuators target large-scale positive fluctuations, the energy of the large-scale structures in the log-region have been reduced. A reversed phenomenon occurs if the actuation is upon the low-speed zones, in this case the *reinforcing* control actually strengthens the large-scale fluctuations. For the case of *desynchronised* control the large-scale structures retain their original energy distribution, which is potentially the average effect of half of the time having an *opposing* control scheme, and the other half having a *reinforcing* control scheme.

4. Control effects at $d_a = 1.7\delta$ downstream of actuation

All results that follow were measured at a distance $d_a \approx 1.7\delta$ downstream of actuation. For this location we observed the maximum effect of the *opposing* control scheme.

4.1. Mean velocity and turbulence intensity profiles

The mean streamwise velocity and streamwise turbulence intensity profiles of both the *uncontrolled* flow and *opposing* controlled TBL are shown in Figs. 6a and b, respectively, for a distance of $d_a/\delta = 1.7$ downstream of actuation. As seen from Fig. 6a, in a mean sense, the wall-normal jet actuators generate a low-speed region from the wall, up to the penetration height (denoted as z_p^+) of the jet airflow into the turbulent boundary layer, which exceeds the upper limit of the log-region, marked in Fig. 6a with a dash-dotted line. The penetration height is determined to be the wall-normal height at which the mean streamwise velocity of the controlled boundary layer reaches 99% of that of the uncontrolled one. Therefore, at the current experimental conditions and with the chosen jet exit velocity ($V_j/U_\infty \approx 0.64$), direct manipulation of the large-scale structures in the log-region is assured. According to Fig. 6b, the turbulence intensity has been reduced from the first point of the boundary layer measurement ($z^+ \approx 8.6$) until a wall-normal height of $z/\delta \approx 0.08$, above which there is an increase in the turbulence intensity. This increase diminishes when reaching the penetration height z_p^+. In the next section (Section 4.2) we will reveal that the increase in turbulence intensity near the upper

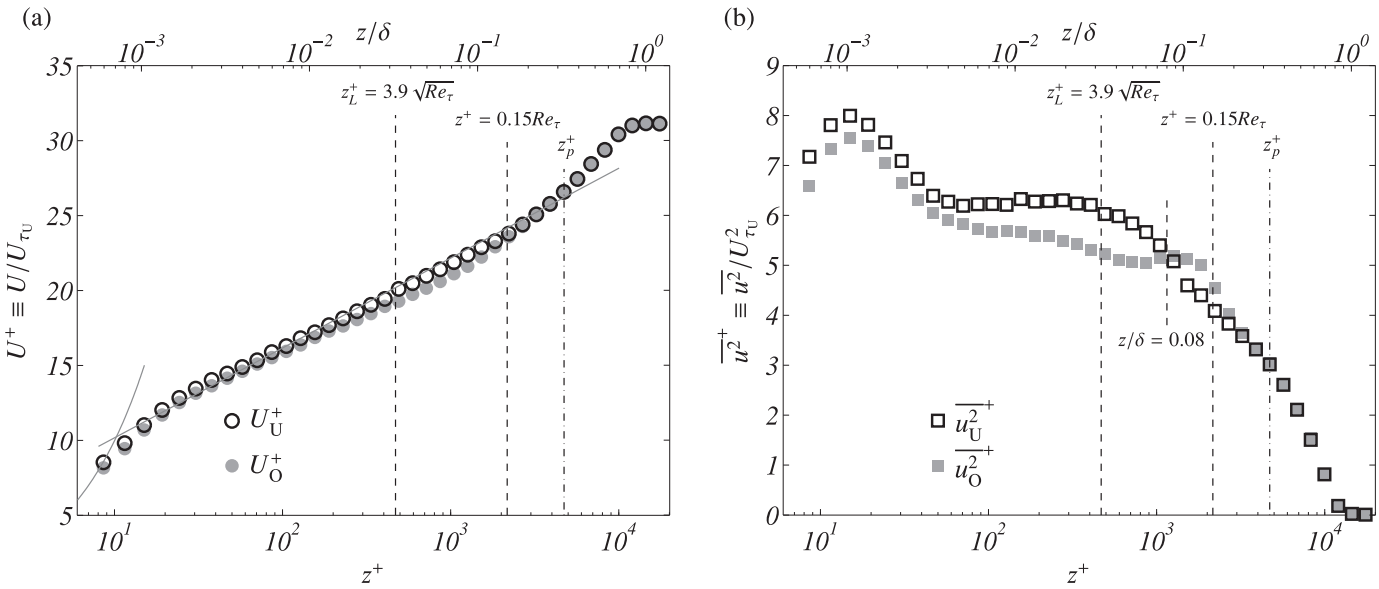

Fig. 6. (a) Mean velocity profile at $d_a/\delta \approx 1.7$ downstream of the actuation at $y = 0$ for the *uncontrolled* flow and the *opposing* control scheme. Dashed lines mark position z_L^+ and the outer-edge of the log-region ($z^+ = 0.15Re_\tau$). A dash dotted line marks the penetration depth of the actuator-flows, described in the text. (b) Similar to sub-figure (a) but for the streamwise turbulence intensity.

limit of the log-region may be attributed to the small-scale energy created at the edge of the jets in cross-flow.

4.2. Boundary layer energy spectrograms

Figs. 7a and b show contours of the pre-multiplied energy spectra throughout the boundary layer (referred to as a 'spectrogram') for the *uncontrolled* ($k_x\phi_{uu_U}/U_{\tau_U}^2$), and *opposing* controlled ($k_x\phi_{uu_O}/U_{\tau_U}^2$) TBL flows, respectively.

For the *uncontrolled* case in Fig. 7a two energetic peaks are observed (shown by the two black plus symbols); (i) an inner-peak at $z^+ \approx 12$, $\lambda_x^+ \approx 1000$ corresponding to the near-wall cycle of streaks and quasi-streamwise vortices, and (ii) an energetic outer-peak located nominally at $z_L^+ \equiv 3.9\sqrt{Re_\tau}$ and $\lambda_x \approx 3\delta$, corresponding to LSMs and superstructures in the log-region (Hutchins and Marusic, 2007a). The most discernible feature of the spectrogram in Fig. 7b is the diminished outer-peak. To highlight the changes to the energy content caused by the *opposing* control scheme, the differences of Figs. 7a and b are shown in an absolute and relative (percentage) sense in Figs. 7c and d, respectively. Adjacent to the colour bars we have indicated how the contours were computed. The cut-off wavelength of the large-scale filter, as well as the penetration depth of the actuator-flows (as discerned from Fig. 6a) are also shown. It is clear that the region of diminished large-scale energy (negative-valued regions in Figs. 7c and d) is largely restricted to wavelengths $\lambda_x > \lambda_{xF}$, demonstrating that the controller is successfully targeting the specified large-scale zones. Likewise, in the wall normal direction, it is clear that this alteration of large-scale energy only occurs up to approximately one-third of the penetration depth z_p^+.

The relatively intense increase in the energy (positive-valued regions in Figs. 7c and d) is believed to be related to small-scale turbulence activity at the upper-edge of the actuator-jet flows penetrating into the TBL flow (as was also observed in an integral-sense as the increase of the turbulence intensity in the case of the opposing control scheme, relative to the uncontrolled flow (around $z^+ \approx 0.15Re_\tau$, see Fig. 6b). Although the highest reduction in spectral energy (more than 30%) was found for wavelengths larger than 5δ and roughly centred around z_L^+, all scales larger than 2δ still comprise an energy reduction of more than 15%, all the way extending down to the wall.

4.3. Conditional large-scale structure

Conditional averages of the large scale structure can be constructed from the full boundary layer profile measurements, of which their statistics were shown in Fig. 6. For each wall-normal position of the hot-wire (profile acquired at $d_a/\delta = 1.7$), the fluctuating signal, $u(z, t)$, is conditioned on zero-crossings in the large-scale voltage signal of the spanwise centred hot-film upstream (sensor s_5). Zero-crossings with a positive temporal gradient are selected (note that exact opposite-sign results would be obtained for negative gradients) and the conditional averaging is performed according to

$$\tilde{u}^+(z,\tau) = \left\langle u(z,t) \;\middle|\; \left(e_L(y_5, t-\tau) = 0 \;\; \& \;\; \ldots \right.\right.$$
$$\left.\left. \ldots \;\; \frac{\partial e_L(y_5, t-\tau)}{\partial t} = 0 \right) \right\rangle. \tag{3}$$

Here, τ is the time coordinate of the conditional velocity and the angular brackets denote an ensemble average over multiple conditional points. A tilde notation denotes the conditional fluctuation. An iso-contour map of $\tilde{u}^+(z,\tau)$ for the *uncontrolled* flow and *opposing* control scheme are shown in Figs. 8a and b, respectively. Seemingly, Fig. 8a demonstrates the forward inclination of the LSMs and their coherent nature in wall-normal direction. For the *opposing* control case it is observed that a large portion of the conditional high-speed zone is reduced in amplitude.

Although boundary layer surveys are obtained for the *uncontrolled* and *opposing* controlled cases only, we have conditioned fluctuations for all control schemes available in the log-region at z_L^+, which are shown in Fig. 8c. Negligible change of the conditional profile for the *desynchronised* scheme, in comparison to the *uncontrolled* case, is observed, which reflects our earlier observation of the spectra (Fig. 5b). For the *opposing* control case the relative amplitudes of both the high- and low-speed zones have been diminished. The reversed effect is observed for the *reinforcing* control case. These findings are again in agreement with the observed

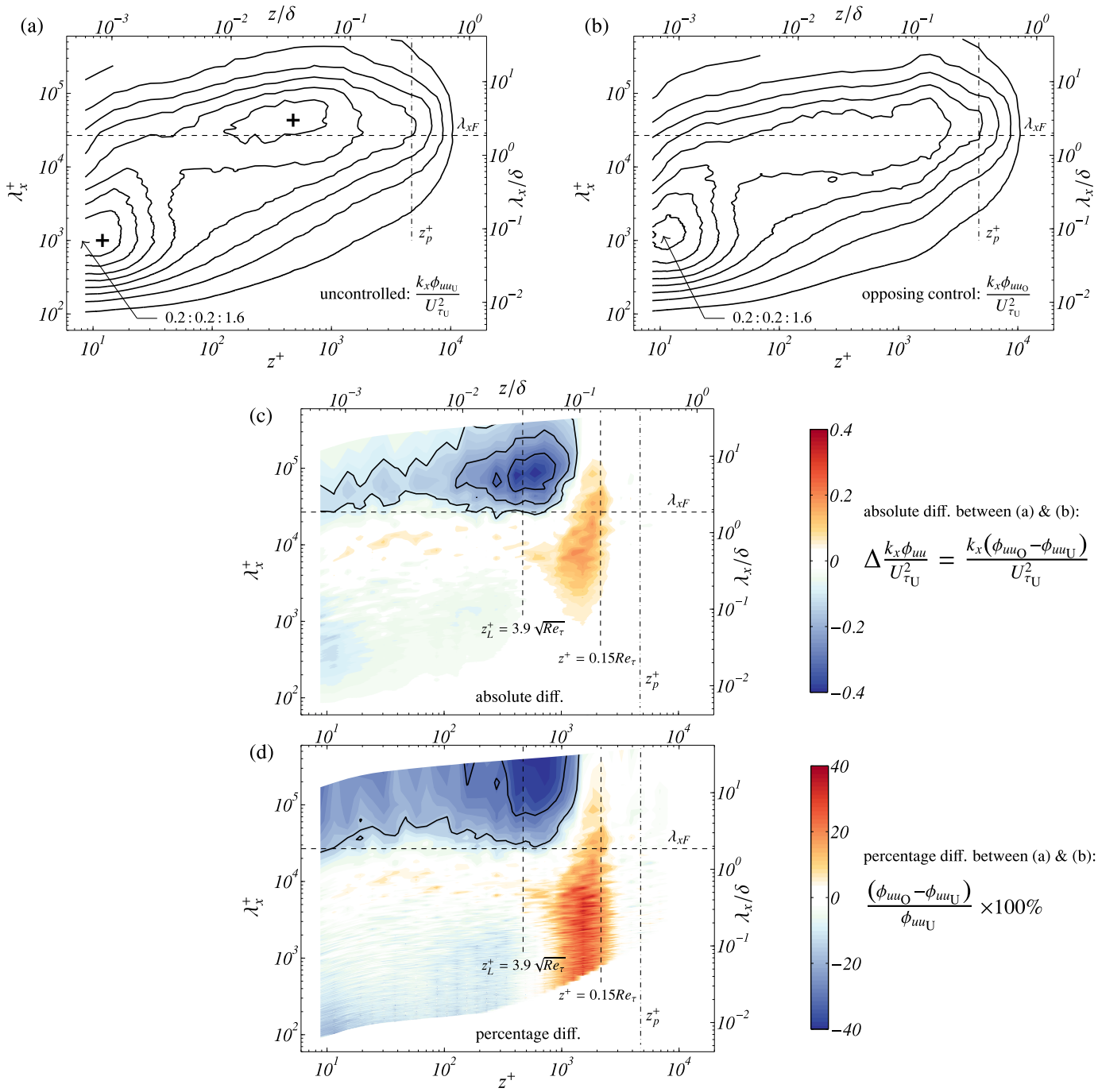

Fig. 7. (a,b) Contours of the pre-multiplied energy spectra of the streamwise velocity fluctuations, $k_x\phi_{uu}/U_{\tau_U}^2$, for the *uncontrolled* and *opposing* control scheme, respectively (level range 0.2–1.6, level step 0.2). (c,d) Absolute and percentage difference of the energy spectrograms presented in subfigures (a) and (b); negative values indicate an energy reduction due to the *opposing* control scheme, relative to the *uncontrolled* TBL flow. Black contours in sub-figure (c) correspond to levels of −0.1, −0.2 and −0.3, whereas the black contours in (d) are associated with levels −15 and −30.

decrease and increase of the large-scale energy in Fig. 5b, for the *opposing* and *reinforcing* control cases, respectively.

4.4. Mean wall-shear stress

Here we examine the effect of the control on the mean wall-shear stress, τ_w, here referred to as 'drag'. Fig. 9 shows the percentage reduction in skin-friction drag for all three control schemes, measured by hot-film sensor s_5', located $d_a/\delta \approx 1.7$ downstream—and in the spanwise centre of—the actuator-array. Drag reduction has been observed for all three schemes (indicated with a numerical value above each respective bar). The error bars correspond to the 95% confidence interval of twenty measurement points that were acquired per scheme. Each measurement point relates to the mean value of a 180 s long signal, which was calibrated according to the procedure described in Appendix A.

As shown in Section 3, the energy of the large-scale structures in the log-region has not been altered for the *desynchronised* scheme. Hence, the 2.4% drag reduction for the *desynchronised* control case can be attributed to the generated-low-momentum re-

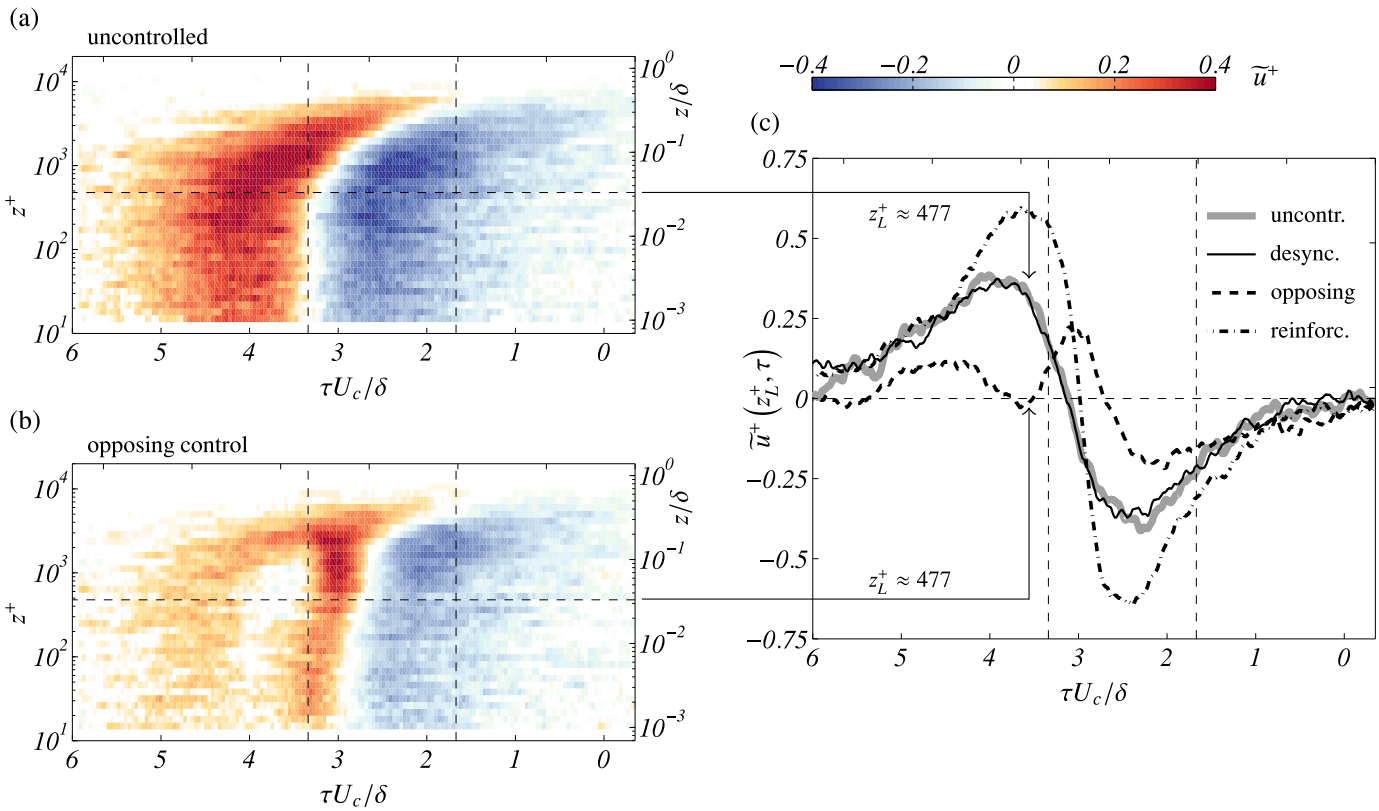

Fig. 8. (a,b) Iso-contours of the conditional streamwise velocity fluctuations, $\widetilde{u}^+(z,\tau)$, throughout the boundary layer at $d_a/\delta = 1.7$ downstream of the actuation, conditioned on zero-crossings in the footprint of the large-scale fluctuations at the wall, following Eq. (3), for both the (a) *uncontrolled* flow and (b) *opposing* control case. Vertical dashed lines are drawn at $\tau U_c/\delta = \Delta x/\delta$ and $\tau U_c/\delta = 2\Delta x/\delta$ (note that $d_a/\delta \approx 1.7$ is located $2\Delta x/\delta$ downstream of the conditioning point, sensor s_5). (c) Profiles of the conditionally averaged streamwise velocity fluctuations at $z_L^+ \equiv 3.9\sqrt{Re_\tau}$ for the *uncontrolled* flow and all three control schemes.

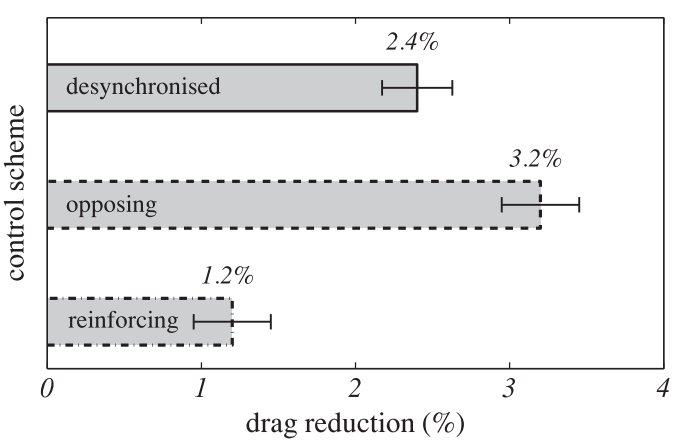

Fig. 9. Percentage skin-friction drag reduction at $d_a = 1.7\delta$ downstream of actuation and $y = 0$. Error bars for the *desynchronised*, *opposing* and *reinforcing* scheme have magnitudes of 0.45%, 0.50% and 0.50%, respectively, and correspond to the 95% confidence interval of the measurement.

gion downstream of the wall-normal actuator-flow. In other words, the wall-normal jet actuation, regardless of the synchronisation between the actuation and the incoming structure, injects fluid without any streamwise momentum into the TBL. Possibly, the wall-normal jet flows can lift incoming fluid with streamwise momentum away from the surface, thereby reducing the streamwise velocity gradient at the wall (and hence the skin-friction drag). A greater skin-friction drag reduction of 3.2% is observed for the *opposing* control scheme. The additional portion of the drag reduction are related to the less energetic large-scale high-speed zones, which exert positive wall-shear stress fluctuations. Accordingly, the mechanism of the drag reduction of the control scheme can be explained as a combination of the beneficial effects of both the streamwise momentum deficit generated via the wall-normal jet actuation and the energy decrease of the large-scale structures which results in a weaker influence on the wall. For the reinforcing control case, which strengthens the large-scale fluctuations, a skin-friction drag reduction of 1.2% is observed, approximately half of that observed during the *desynchronised* case. Together, despite the relatively minor changes in skin-friction drag, the results seem to suggest a clear link between the large-scale energy and the magnitude of the wall shear stress.

5. Concluding remarks

The energetic large-scale structures in the log-region of a high-Reynolds-number TBL ($Re_\tau \approx 14\,400$) were experimentally manipulated. A spanwise array of nine wall-normal jets was employed as actuators and operated in on/off mode with an exit velocity that causes the jets in cross-flow to penetrate within the log-region. Each jet was triggered in real-time with an active controller, driven by a time-resolved footprint of the large-scale motions acquired upstream.

When on-periods of the actuators are synchronised with large-scale high-speed zones in the TBL flow (*opposing* control) the relative amplitudes of both the high- and low-speed zones in the log-region are mitigated following an opposition mechanism. This decrease in streamwise turbulence intensity in the log-region is persistent for a reasonably large distance, the evidence of which is observed even at 5δ downstream of the actuators. The highest reduction in spectral energy—more than 30%—was found for wave-

lengths larger than 5δ in the log-region at 1.7δ downstream of actuation, while scales larger than 2δ still comprised more than 15% energy reduction in the near-wall region. Additionally, 3.2% skin-friction drag reduction has been achieved at 1.7δ downstream of the actuation location, a quarter of which may be attributed to synchronizing the jet actuation to the naturally occurring high-speed large-scale motions. That is, three-quarters of the 3.2% skin-friction drag reduction can be attributed to the streamwise momentum deficit that was generated downstream of the injected jet fluid by the actuators, since a 2.4% ($= 3/4 \cdot 3.2\%$) skin-friction drag reduction was obtained when the actuators operated via a *desynchronised* control scheme. For such type of manipulation, no defined synchronization between the actuation and any of the incoming large-scale structures are prescribed. Consequently, half of the actuation would be upon the high-speed zones and the other half would be upon the low-speed zones. In an effort to study the response of the TBL to external large-scale perturbations even further, a *reinforcing* control scheme was implemented, in which the jet actuation was synchronised with the low-speed zones. Despite the fact that an increase in the energy of the large-scale structures in regions above the near-wall region has been observed due to such manipulation, 1.2% skin-friction drag reduction was measured at 1.7δ downstream of the actuators. It can therefore be speculated that the measured drag reduction is an amalgamate influence of the following two factors: 1) the beneficial effect of the low-momentum region generated downstream of the actuators induced by the wall-normal jet actuators and, 2) the detrimental top-down effect of the more energetic large-scale structures in the regions above the near-wall region; where the former factor overpowers the latter one.

Acknowledgements

This paper is dedicated to Professor Andrew Pollard on the occasion of his retirement; his insights to turbulence and fluid mechanics in general are greatly valued. Appreciation is expressed to Dr. Krishna M. Talluru, Brett J. Bishop and William Ross for insightful discussions and assistance with the experimental hardware. Financial support has been provided by the Australian Research Council.

Appendix A. Calibration of hot-film sensors

A spanwise array of nine hot-films was positioned at $x_5 = 21.00$ m to measure the effects of control (Section 2.4). In order to assess the change in skin-friction drag, these sensors were calibrated so that the mean skin-friction (in terms of an absolute shear-stress or friction velocity) could be inferred.

Since the hot-films were attached to a modular panel insert (made of Aluminium), heat of the sensors could conduct to the underlying surface (note that the hot-films at x_5 were operated in constant-temperature anemometer mode with an overheat ratio of 1.50). Consequently, temperature variations in the laboratory directly influence the output voltages of the sensors. The temperature in the wind tunnel facility, T, was therefore continuously logged during the experiment and used for sensor calibration, which was performed as follows. As for a typical calibration of hot-wire anemometry measurements, the mean voltage of the hot-film was recorded for a sequence of unit Reynolds numbers in our facility (U_∞/ν), corresponding to nominal free-stream velocities of 17 m/s, 18 m/s, 19 m/s, 20 m/s and 21 m/s (at each velocity setting we recorded the sensor for 180 s—the mean of which is referred to as a single realization—resulting in a 0.11% uncertainty in the mean value with a 95% confidence level). Using previously acquired wall-shear stress data at $x_5 = 21.00$ m (Baars et al., 2016b), U_∞/ν could be converted to a unit friction Reynolds number U_{τ_U}/ν (and thus a friction velocity U_{τ_U}), at that particular streamwise location of the hot-film sensor array. From 20 realizations at each of the five velocity settings, calibration data consist of the mean friction velocity (U_{τ_U}), mean voltage (E) and mean temperature (T), which are shown with the circled markers in Fig. A.10a for hot-film sensor s_5'. It was observed that these calibration data obey the following functional form: $U_{\tau_U} = aT + bE + c$, where the coefficients were determined from a linear least squares fitting ($a = 0.122$, $b = 0.312$ and $c = -1.871$; the corresponding planar surface is shown with the mesh in Fig. A.10a). Having obtained how U_{τ_U} depends on the voltage of the hot-film sensor and temperature, the mean value of a modified friction velocity during a case of active control could be inferred from recordings of the respective mean voltage and temperature.

Aside from the calibration recordings, the three control schemes (Table 3) were also operated for 180 s long realizations and re-

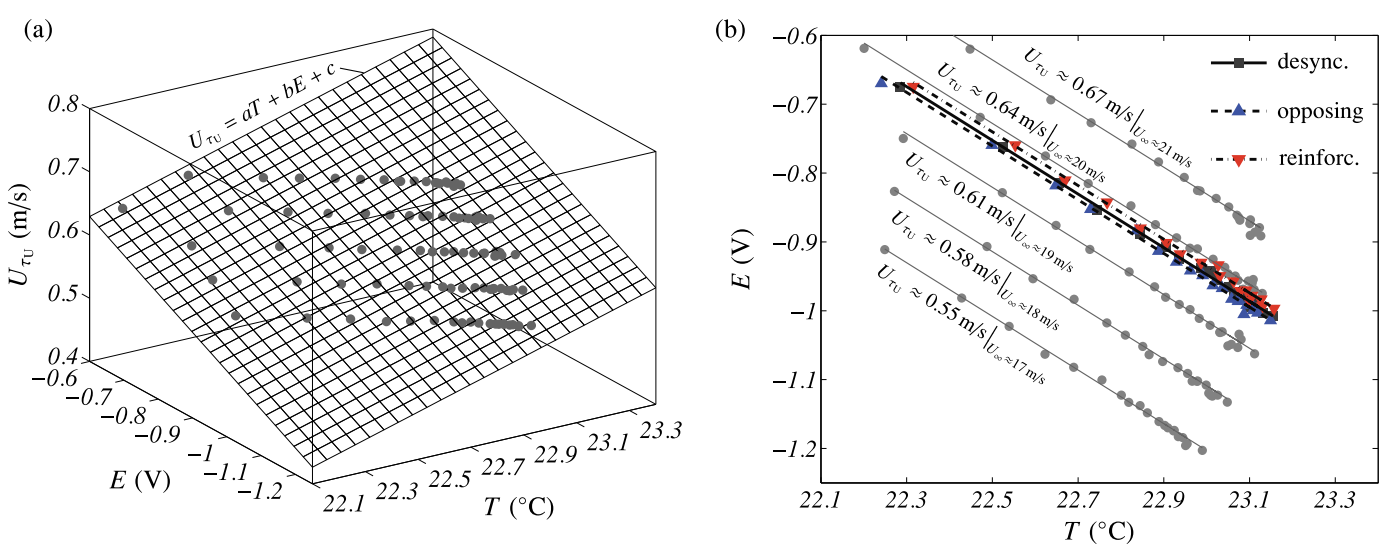

Fig. A.10. (a) Calibration data of one hot-film (sensor s_5'), consisting of the mean friction velocity (U_{τ_U}), mean voltage (E) and mean temperature (T) for five different unit friction Reynolds numbers. A least squares fit of a planar surface to these data is described by $U_{\tau_U} = aT + bE + c$, with $a = 0.122$, $b = 0.312$ and $c = -1.871$. (b) Calibration data of sub-figure (a) projected in the (E, T) plane (circles), alongside the mean voltage and mean temperature recordings of the 20 realizations obtained for each of the three control schemes.

peated 20 times to check for consistency/repeatability and converged statistics of the changes in skin-friction drag (Section 4.4). In practice, the calibration recordings and the control experiments were carried out in an alternating sense. First, the calibration recordings were obtained at nominal free-stream velocities of 17 m/s, 18 m/s, 19 m/s and 20 m/s (4 realizations). Secondly, the three control schemes were recorded at the nominal velocity setting of 20 m/s (3 realizations). Finally, the calibration recording was obtained at 21 m/s (1 realization). This sequence of 8 realizations was then repeated 20 times. For reference, mean quantities of voltage and temperature for all these data are plotted in Fig. A.10b. Here, the five groups of data with the circles correspond to the calibration recordings at the five discrete calibration settings (the corresponding values of U_{τ_U} are provided—essentially a projection of the data from Fig. A.10a in the (E, T) plane). The data points corresponding to the three control schemes lay, on average, below the calibration recordings corresponding to the nominal operating conditions ($U_{\tau_U} \approx 0.639$ m/s), and reflects the skin-friction drag reductions presented in Section 4.4.

References

Abe, H., Kawamura, H., Choi, H., 2004. Very large-scale structures and their effects on the wall shear-stress fluctuations in a turbulent channel flow up to $Re_\tau = 640$. J. Fluids Eng. 126 (5), 835–843.

Adrian, R.J., Meinhart, C.D., Tomkins, C.D., 2000. Vortex organization in the outer region of the turbulent boundary layer. J. Fluid Mech. 422, 1–54.

Baars, W.J., Hutchins, N., Marusic, I., 2016a. Spectral stochastic estimation of high-Reynolds-number wall-bounded turbulence for a refined inner-outer interaction model. Phys. Rev. Fluids 1 (054406), 1–23.

Baars, W.J., Squire, D.T., Talluru, K.M., Abbassi, M.R., Hutchins, N., Marusic, I., 2016b. Wall-drag measurements of smooth- and rough-wall turbulent boundary layers using a floating element. Exp. Fluids 57 (5), 1–16.

Baars, W.J., Talluru, K.M., Bishop, B.J., Hutchins, N., Marusic, I., 2014. Spanwise inclination and meandering of large-scale structures in a high-Reynolds-number turbulent boundary layer. In: 19th Australasian Fluid Mechanics Conference, Melbourne, Australia.

Bai, H.L., Zhou, Y., Zhang, W.G., Xu, S.J., Wang, Y., Antonia, R.A., 2014. Active control of a turbulent boundary layer based on local surface perturbation. J. Fluid Mech. 750, 316–354.

Canton, J., Örlü, R., Chin, C., Schlatter, P., 2016. Reynolds number dependence of large-scale friction control in turbulent channel flow. Phys. Rev. Fluids 1 (081501). R

Chang, Y., Collis, S.S., Ramakrishnan, S., 2002. Viscous effects in control of near-wall turbulence. Phys. Fluids 14 (11), 4069–4080.

Chauhan, K.A., Monkewitz, P.A., Nagib, H.M., 2009. Criteria for assessing experiments in zero pressure gradient boundary layers. Fluid Dyn. Res. 41 (2), 021404.

Dennis, D.J.C., Nickels, T.B., 2011. Experimental measurement of large-scale three-dimensional structures in a turbulent boundary layer. Part 1. Vortex packets. J. Fluid Mech. 673, 180–217.

Gatti, D., Quadrio, M., 2013. Performance losses of drag-reducing spanwise forcing at moderate values of the Reynolds number. Phys. Fluids 25 (12), 125109.

Gouder, K., Potter, M., Morrison, J.F., 2013. Turbulent friction drag reduction using electroactive polymer and electromagnetically driven surfaces. Exp. Fluids 54 (1), 1–12.

Gad-el Hak, M., 1994. Interactive control of turbulent boundary layers – a futuristic overview. AIAA J. 32 (9), 1753–1765.

Gad-el Hak, M., 2000. Flow control: passive, active and reactive flow management. Cambridge University Press.

Gad-el Hak, M., Bandyopadhyay, P.R., 1994. Reynolds number effects in wall-bounded turbulent flows. Appl. Mech. Rev. 47 (8), 307–365.

Head, M.R., Bandyopadhyay, P., 1981. New aspects of turbulent boundary-layer structure. J. Fluid Mech. 107, 297–338.

Hurst, E., Yang, Q., Chung, Y.M., 2014. The effect of Reynolds number on turbulent drag reduction by streamwise travelling waves. J. Fluid Mech. 759, 28–55.

Hutchins, N., Chauhan, K.A., Marusic, I., Monty, J.P., Klewicki, J., 2012. Towards reconciling the large-scale structure of turbulent boundary layers in the atmosphere and laboratory. Bound-Lay. Meteorol. 145 (2), 273–306.

Hutchins, N., Marusic, I., 2007a. Evidence of very long meandering features in the logarithmic region of turbulent boundary layers. J. Fluid Mech. 579, 1–28.

Hutchins, N., Marusic, I., 2007b. Large-scale influences in near-wall turbulence. Phil. Trans. R. Soc. A 365 (1852), 647–664.

Hutchins, N., Monty, J.P., Ganapathisubramani, B., Ng, H.C.H., Marusic, I., 2011. Three-dimensional conditional structure of a high-Reynolds-number turbulent boundary layer. J. Fluid Mech. 673, 255–285.

Hutchins, N., Nickels, T.B., Marusic, I., Chong, M.S., 2009. Hot-wire spatial resolution issues in wall-bounded turbulence. J. Fluid Mech. 635, 103–136.

Iwamoto, K., Suzuki, Y., Kasagi, N., 2002. Reynolds number effect on wall turbulence: toward effective feedback control. Int. J. Heat. Fluid Flow 23 (5), 678–689.

Johansson, A.V., Alfredsson, P.H., 1982. On the structure of turbulent channel flow. J. Fluid Mech. 122, 295–314.

Karniadakis, G.E., Choi, K.-S., 2003. Mechanisms on transverse motions in turbulent wall flows. Annu. Rev. Fluid Mech. 35 (1), 45–62.

Kasagi, N., Suzuki, Y., Fukagata, K., 2009. Microelectromechanical systems-based feedback control of turbulence for skin friction reduction. Annu. Rev. Fluid Mech. 41, 231–251.

Kim, J., Moin, P., 1979. Large-eddy simulation of turbulent channel flow. NASA Tech. Memo. 78619.

Kline, S.J., Reynolds, W.C., Schraub, F.A., Runstadler, P.W., 1967. The structure of turbulent boundary layers. J. Fluid Mech. 30 (4), 741–773.

Ligrani, P.M., Bradshaw, P., 1987. Spatial resolution and measurement of turbulence in the viscous sublayer using subminiature hot-wire probes. Exp. Fluids 5 (6), 407–417.

Marusic, I., Chauhan, K.A., Kulandaivelu, V., Hutchins, N., 2015. Evolution of zero–pressure-gradient boundary layers from different tripping conditions. J. Fluid Mech. 783, 379–411.

Marusic, I., Mathis, R., Hutchins, N., 2010a. High Reynolds number effects in wall turbulence. Int. J. Heat Fluid Flow 31 (3), 418–428.

Marusic, I., Mathis, R., Hutchins, N., 2010b. Predictive model for wall-bounded turbulent flow. Science 329 (5988), 193–196.

Marusic, I., Monty, J.P., Hultmark, M., Smits, A.J., 2013. On the logarithmic region in wall turbulence. J. Fluid Mech. 716, R3.

Mathis, R., Hutchins, N., Marusic, I., 2009. Large-scale amplitude modulation of the small-scale structures in turbulent boundary layers. J. Fluid Mech. 628, 311–337.

Moin, P., Bewley, T., 1994. Feedback control of turbulence. Appl. Mech. Rev. 47 (6s), S3–S13.

Nickels, T.B., Marusic, I., Hafez, S., Chong, M.S., 2005. Evidence of the k_1^{-1} law in a high-Reynolds-number turbulent boundary layer. Phys. Rev. Lett. 95 (7), 074501.

Nikuradse, J., 1933. Laws of flow in rough pipes. NASA Tech. Memo., 1292.

Rathnasingham, R., Breuer, K.S., 1997. System identification and control of turbulent flows. Phys. Fluids 9, 1867–1869.

Rathnasingham, R., Breuer, K.S., 2003. Active control of turbulent boundary layers. J. Fluid Mech. 495, 209–233.

Robinson, S.K., 1991. The kinematics of turbulent boundary layer structure. NASA Tech. Memo. 103859.

Schoppa, W., Hussain, F., 1998. A large-scale control strategy for drag reduction in turbulent boundary layers. Phys. Fluids 10 (5), 1049–1051.

Smits, A.J., Marusic, I., 2013. Wall-bounded turbulence. Phys. Today 66 (9), 25.

Talluru, K.M., Kulandaivelu, V., Hutchins, N., Marusic, I., 2014. A calibtration technique to correct sensor drift issues in hot-wire anemometry. Meas. Sci. Technol. 25, 105304.

Townsend, A.A., 1976. The Structure of Turbulent Shear Flow. Cambridge University Press.

Wark, C.E., Nagib, H.M., 1990. Relation between outer structures and wall-layer events in boundary layers with and without manipulation. In: Structure of Turbulence and Drag Reduction, pp. 467–474.